Nanoscale

PAPER

View Article Online
View Journal | View Issue

Check for updates

Cite this: *Nanoscale*, 2019, **11**, 8803

The dealloying–lithiation/delithiation–realloying mechanism of a breithauptite (NiSb) nanocrystal embedded nanofabric anode for flexible Li-ion batteries†

Renpeng Chen,[a] Xiaolan Xue,[a] Jingyu Lu,[a] Tao Chen,[a] Yi Hu,[a] Lianbo Ma,[a] Guoyin Zhu[a] and Zhong Jin *[a,b]

Received 6th January 2019,
Accepted 31st March 2019

DOI: 10.1039/c9nr00159j

rsc.li/nanoscale

Antimony (Sb) based anodes with high conductivity and capability have shown great promise for applications in lithium ion batteries (LIBs). However, they often suffer from poor cycling stability because of the drastic volume variation and structural degradation on undergoing lithiation–delithiation processes. Here we demonstrate a novel Sb-based anode with a free-standing structure realized by uniformly implanting intermetallic compound breithauptite (nickel antimonide, NiSb) nanocrystals into nitrogen-doped carbon nanofibers (NiSb@NCNFs). The discharge/charge behavior of NiSb@NCNFs was systematically investigated by *ex situ* characterization, which revealed a special "dealloying–lithiation/delithiation–realloying" cycling mechanism. The NiSb nanocrystals possess high lithium storage capacity, and the interconnected network of NCNFs can accommodate the volume variation of encapsulated NiSb nanoparticles, while also providing smooth pathways for charge transport. Compared to other Sb-based anodes, the NiSb@NCNF anode presents exceptional reversible capacity (720 mA h g^{-1} at a current density of 100 mA g^{-1}) and greatly enhanced cycling life at high rates (510 mA h g^{-1} after 2000 cycles at 2000 mA g^{-1}). Furthermore, the free-standing NiSb@NCNF anode is free of binders, conductive additives and metal current collectors, exhibiting high flexibility and remarkable performances for the construction of flexible and bendable soft-packed full Li-ion pouch cells.

Introduction

To provide sufficient power supply for wearable electronic devices, it is crucial to develop energy storage devices with high capacity, good flexibility and long cycling life.[1–10] Although lithium ion batteries (LIBs) have exhibited remarkable performances, such as decent energy density, low self-discharge rate and no memory effect, the low theoretical specific capacity of traditional graphite-based anodes (372 mA h g^{-1}) cannot meet the booming demands,[11] and the low lithiation potential of graphite may cause safety issues due to the formation of lithium dendrites.[12–14] Moreover, the practical deployment of flexible Li-ion batteries suffers from the poor mechanical strength and flexibility of electrode materials, which may lead to significantly decreased conductivity and capacity upon repeated deformation. Therefore, it is crucial to design next-generation anode materials that can simultaneously meet the capacity, stability and flexibility requirements for flexible Li-ion batteries.

In recent years, various lithium storage materials, such as transition metal compounds,[15–19] and group IV and group V materials (Si,[20] Ge,[21] Sn,[22,23] and Sb[24]) have been regarded as promising candidates for anode materials. Notably, Sb has attracted increasing interest because of its remarkable conductivity (~100 times higher than Si), decent theoretical capacity (660 mA h g^{-1}) and safe operation potential (about 0.5–0.8 V *vs.* Li/Li$^+$). However, Sb also suffers from several shortcomings, especially the large volume expansion during lithiation that may break the already formed solid–electrolyte interface (SEI) film, resulting in further consumption of organic electrolytes and the formation of a thicker SEI film.[25] In this case, the conductivity and coulombic efficiency of Sb-based anodes tend to rapidly decrease during discharge–charge processes, resulting in poor cycling life.[26–29] Recently, great efforts have been made to improve the performance of Sb-based anodes through the design of Sb based compounds or composites (as listed in Table S1†).[30–39] However, the specific capacity and cycling life

---

[a] *Key Laboratory of Mesoscopic Chemistry of MOE, Jiangsu Key Laboratory of Advanced Organic Materials, School of Chemistry and Chemical Engineering, Nanjing University, Nanjing 210023, China. E-mail: zhongjin@nju.edu.cn*
[b] *Shenzhen Research Institute of Nanjing University, Shenzhen 518063, China*

† Electronic supplementary information (ESI) available. See DOI: 10.1039/c9nr00159j

of Sb-based anodes are still not very satisfactory. On the other hand, the production of electrodes normally requires polymer binders, conductive additives (*e.g.* carbon black) and current collectors that reduce the overall specific capacity and flexibility. The polymer binders, such as polyvinylidene fluoride (PVDF), are usually insulating and hinder electron/ion transport.[40,41] Therefore, it is of great importance to find new strategies for the design and fabrication of flexible anodes.

Considering that the architecture of electrode materials is a key factor to their performance, we propose that an advanced Sb-based anode can be created by embedding antimonide nanocrystals into a three-dimensional (3D) interconnected carbon scaffold, which brings the following advantageous features: (1) the antimonide nanocrystals homogeneously dispersed in the carbon scaffold guarantee a high electrochemically active surface area and a high utilization ratio; (2) the porous carbon scaffold can buffer the volume change of encapsulated nanocrystals and prevent the structural fragmentation during cycling processes; (3) the SEI film can be formed on the outer surface of the carbon shell, alleviating the side reactions of the active material with the electrolyte; and (4) the conductive network of the carbon scaffold ensures the expedited transport of electrons and ions, avoiding the use of polymer binders, conductive additives or current collectors, and thus can reduce the weight of batteries. Therefore, there are many predictable merits associated with designing of novel Sb/C-based composite anodes with all the above features. Following this line of thought, here we report an effective strategy to fabricate breithauptite (nickel antimonide, NiSb) nanocrystal encapsulated nitrogen-doped carbon nanofibers (NiSb@NCNFs) as a flexible, binder-free and current collector-free anode for LIBs (Scheme 1a). The breithauptite particles in hexagonal crystalline symmetry have remarkable lithium storage capacity and exhibit a special "dealloying–lithiation/delithiation–realloying" mechanism during the cycling processes (Scheme 1b). Moreover, the intertwined NCNFs are very effective at accommodating the volume change of the active material and providing an integrated conductive network for smooth charge transfer.[42–47] Consequently, when assembled into full cells or flexible pouch cells, the NiSb@NCNF anode exhibits high capacity, flexibility and long-term cycling stability at high current densities.

Experimental

Material synthesis

The NiSb@NCNF electrode was obtained through an electrospinning route followed by a thermal treatment process. Typically, 1.0 g of polyacrylonitrile (PAN) was added into 8.0 mL of *N*,*N*-dimethylformamide (DMF) solution under vigorous stirring for 1 h at 80 °C. Subsequently, 3.0 mmol of antimony trichloride ($SbCl_3$) and 3.0 mmol of nickel chloride hexahydrate ($NiCl_2 \cdot 6H_2O$) were successively added into the PAN solution, and then kept stirring for another 1 h at 80 °C to obtain a homogeneous precursor solution. The above precursor solution was placed into a 5.0 mL plastic syringe equipped with a blunt stainless-steel syringe needle (inner diameter: 0.5 mm). The distance between the syringe needle and a rolling collector was set to 14 cm, and a high voltage of 20 kV was applied between the syringe needle and a rolling collector to initiate the electrospinning. The flow rate of the precursor solution was kept at 0.15 mL h^{-1}, controlled by a syringe pump. Finally, the nanofabric electrode was obtained from the collector by electrospinning for 6 h at room temperature. The as-prepared nanofabric film was firstly stabilized at 250 °C for 5 h at a heating rate of 2 °C min^{-1}, and then followed by annealing at 700 °C for 1 h at a ramping rate of 5 °C min^{-1} under high-purity N_2 flow.

For comparison, a pristine NCNF electrode (without encapsulated NiSb nanoparticles) was prepared as a control sample in the same way as NiSb@NCNFs but without the addition of

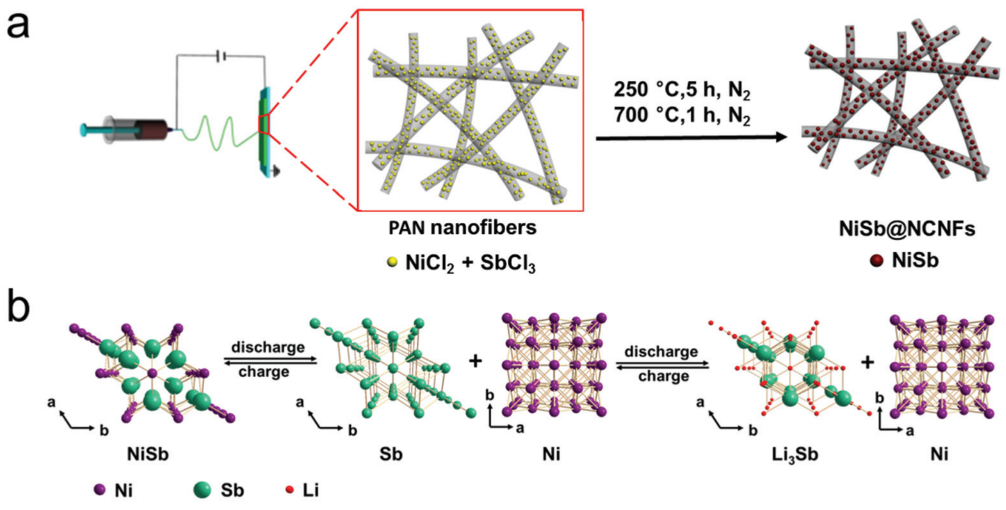

Scheme 1 (a) Schematic preparation process of the NiSb@NCNF anode. (b) Schematic illustration of the crystallographic changes and "dealloying–lithiation/delithiation–realloying" mechanism of NiSb nanocrystals during discharge/charge processes.

Ni- and Sb-based salts. The contents and weight ratios of Ni and Sb elements in the composite electrode can also be changed by adjusting the molar numbers of the $SbCl_3$ and $NiCl_2·6H_2O$ precursors, as discussed in the ESI.† Ni@NCNFs and Sb@NCNFs were also synthesized as control samples by separately adding 6 mmol of $NiCl_2·6H_2O$ or 6 mmol of $SbCl_3$ into the PAN/DMF solution, respectively.

Material characterization

The crystalline structures of the as-prepared nanofabric electrodes were characterized by powder X-ray diffraction (XRD) on an X-ray diffractometer (Bruker D-8 Advance) with a Cu Kα (λ = 1.5406 Å) radiation source. The morphology was identified by field-emission scanning electron microscopy (SEM) on a JEOL JSM-6480 scanning electron microscope. The structural features of the samples were studied on a JEOL JEM-2100F transmission electron microscope at an accelerating voltage of 200 kV. Raman spectra were obtained on a Horiba JY Raman spectrometer using a 473 nm laser source. X-ray photoelectron spectroscopy (XPS, PHI-5000 VersaProbe) was used to analyze the nitrogen-doping configurations in the samples. Nitrogen adsorption–desorption isotherms were obtained through Brunauer–Emmett–Teller (BET) analysis at 77 K on a Quantachrome Autosorb-IQ-2C instrument, and the nitrogen desorption temperature was 300 °C. The Barrett–Joyner–Halenda (BJH) method was used to obtain the pore size distribution from the adsorption branches of the isotherms. Inductively coupled plasma optical emission spectroscopy (ICP-OES, Optima 5300DV) was used to determine the mass contents of Ni and Sb by dissolving the samples in aqua regia. The weight contents of NiSb and NCNFs were measured by thermo-gravimetric analysis (TGA) on a Mettler Toledo SDTA851e analyzer after heating from ambient temperature to 800 °C in air with a ramp rate of 5 °C min^{-1}.

Electrochemical measurements

The CR2032 coin cells were assembled in an argon-filled glovebox. The nanofabric electrodes were cut into round pieces with a diameter of 14 mm, which were directly assembled into the cells without mechanical milling or slurry coating steps. Neither any additives (Ketjen black, polymer binder) nor metal current collectors were used, because the nanofabric electrodes were binder-free and with excellent conductivity. The coin cells were assembled with NiSb@NCNFs as the working electrode, lithium foil as the counter electrode and a Celgard-2400 membrane as the separator. A solution of 1.0 M $LiPF_6$ in the co-solvent of ethylene carbonate (EC) and dimethyl carbonate (DMC) (1 : 1 by volume) was used as the electrolyte. Galvanostatic discharge–charge tests were performed between 0.01 and 3.0 V *vs.* Li/Li^+ at various current densities on a LAND battery-test instrument (CT2001A). All the applied current densities and specific capacities mentioned in this study were based on the total mass of NiSb@NCNFs, and the areal density of the electrodes is around 2.0 mg cm^{-1}. Electrochemical impendence spectroscopy (EIS) and cyclic voltammetry (CV) tests were conducted on a Chenhua CHI-760E electrochemical workstation. The soft-packed full batteries were assembled with a freestanding NiSb@NCNF electrode as the anode, glass fiber (Whatman) as the separator, and $LiFePO_4$ coated Al foil as the cathode, and sealed by Al plastic films. Before assembly, the NiSb@NCNF electrode was prelithiated by attaching the NiSb@NCNF electrode and lithium foil together in a glovebox and then immersing in the electrolyte for 6 h. And the mass ratio of the NiSb@NCNF anode and $LiFePO_4$ cathode was set to approximately 1 : 3.

Results and discussion

Scheme 1a presents the preparation of the NiSb@NCNF anode through an electrospinning process of polyacrylonitrile (PAN) solution mixed with Ni- and Sb-containing salts, following by a two-step annealing process (more details can be found in the Experimental section). The nanoparticles of Ni and Sb salts were embedded in the PAN nanofibers to form a piece of flexible nonwoven nanofabric. During the first annealing step, the precursor PAN nanofibers were stabilized because of the conversion of thermoplastic PAN to a non-plastic or ladder compound.[43] In the second annealing step, the precursor nanofabric was completely carbonized, and the nickel dichloride ($NiCl_2$) and antimony trichloride ($SbCl_3$) precursors were reduced to breithauptite (NiSb) nanocrystals by the carbon at 700 °C. Moreover, a large number of nitrogen species in PAN nanofibers were still retained in the NCNFs, thus providing a high nitrogen doping content for the NCNFs.

The morphology and microstructures of the as-prepared NiSb@NCNF nanofabric electrode were systematically characterized. As shown in the scanning electron microscopy (SEM) images (Fig. 1a and b), the unannealed NiSb@NCNF precursor nanofibers present a homogeneous fibrillar structure with an

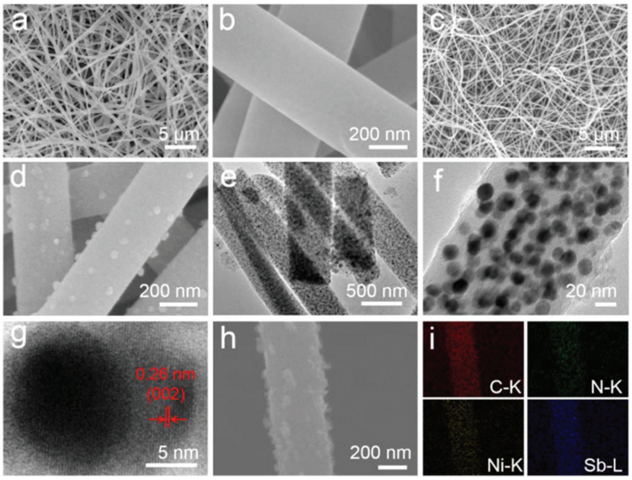

Fig. 1 (a and b) SEM images of the precursor nanofabric before annealing. (c and d) SEM and (e and f) TEM images of the as-prepared NiSb@NCNFs. (g) HRTEM image of an encapsulated breithauptite nanocrystal in NiSb@NCNFs. (h) SEM image and (i) corresponding C, N, Ni and Sb elemental mappings of NiSb@NCNFs.

average diameter of ~500 nm, and the surface is smooth and clear without any attached nanoparticles. After annealing, the final product preserved the uniform nanofibrous structure with a reduced diameter of ~400 nm, and the outer surface of NiSb@NCNFs became rough, owing to the formation of numerous carbon nanoparticles during the calcination process (Fig. 1c and d). The transmission electron microscopy (TEM) images of NiSb@NCNFs (Fig. 1e and f) show the breithauptite nanocrystals homogeneously dispersed inside the NCNFs with an average diameter of ~15 nm due to the added appropriate amounts of nickel and antimony precursors, and also reveal that the larger particles on the outer surface of NiSb@NCNFs are not NiSb but carbon (as shown in the bottom-right corner of Fig. 1f). The high-resolution TEM image of a breithauptite nanocrystal (Fig. 1g) presents a highly ordered lattice fringe of 0.26 nm, corresponding to the (002) planes of NiSb. Energy-dispersive X-ray spectroscopy (EDX) elemental mappings (Fig. 1h and i) and survey X-ray photoelectron spectroscopy (XPS) analysis (Fig. S1†) of NiSb@NCNFs confirm the existence of C, N, Ni and Sb elements. The X-ray diffraction (XRD) pattern of NiSb@NCNFs (Fig. 2a) confirms the diffraction peaks of carbon and breithauptite phase NiSb (JCPDS card no. 41-1439), and no obvious peaks of Ni metal, Sb metal or other Ni_xSb_y phases were found. The D band and G band in the Raman spectrum of NiSb@NCNFs (Fig. 2b) are located at 1357 cm^{-1} and 1583 cm^{-1}, respectively, showing an intensity ratio (I_D/I_G) of ~1.02, corrsponding to the partically disordered carbon structure in NCNFs. The high-resolution XPS spectra in the N 1s region of NiSb@NCNFs (Fig. 2c) can be deconvoluted to three peaks centered at 398.4 eV (pyridinic-N), 399.8 eV (pyrrolic-N) and 400.7 eV (graphitic-N), respectively. The areal percentages of these peaks are calculated to be 61.0%, 21.3% and 17.7%, respectively, demonstrating the dominating atomic ratio of pyridinic N. Similarly, the XPS spectrum in the C 1s region (Fig. 2d) reveals that the areal intensity ratio of C=C, C=N and C–N bonds is 61.2%, 27.8%, and 11.0%, respectively. The nitrogen adsorption–desorption isotherms of NiSb@NCNFs present a type-IV shape (Fig. 2e), implying the abundant mesopores in the nanofibers. The surface area of NiSb@NCNFs was found to be 7.75 m^2 g^{-1}, and the average pore size is ~3.8 nm (Fig. 2f). In contrast, the unannealed NiSb@NCNF precursor presents a very low surface area of 0.89 m^2 g^{-1} and almost no porosity. Thus, the formation of mesopores in the NiSb@NCNFs should be ascribed to the pyrolyzation of PAN during the annealing process. Through the measurements using inductively coupled plasma optical emission spectroscopy (ICP-OES), the total mass content of Ni and Sb was determined to be approximately 45.3 wt% with a Ni/Sb molar ratio of ~1.02 : 1. Thermogravimetric analysis (TGA) was also carried out to identify the weight ratio of Ni and Sb (as detailed in Fig. S2†). The weight change of ~44.0 wt% after heating from ambient temperature to 800 °C in air was attributed to the decomposition of NCNFs and the oxidation of NiSb. Therefore, the content of NiSb was estimated to be approximately 42.7 wt%, which is comparable to the results of ICP-OES.

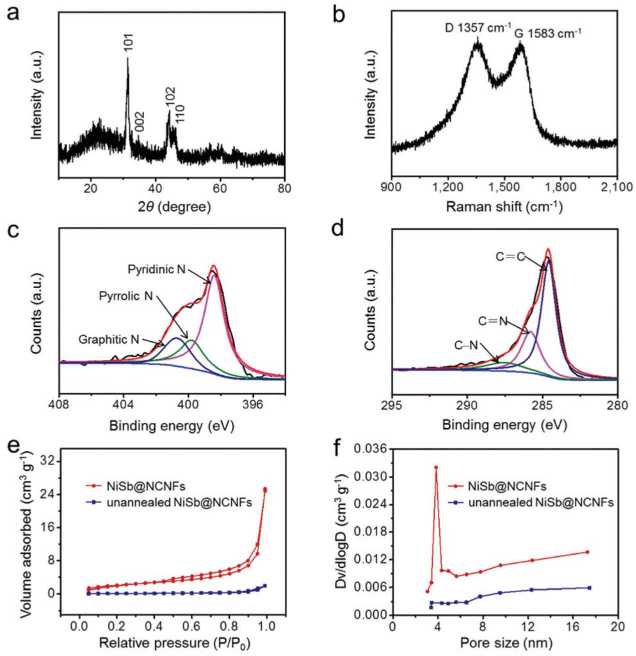

Fig. 2 (a) XRD pattern, (b) Raman spectrum, and (c and d) high-resolution XPS spectra in (c) N 1s and (d) C 1s regions of NiSb@NCNFs. (e) Nitrogen adsorption–desorption isotherms and (f) pore size distribution of NiSb@NCNFs and the unannealed NiSb@NCNF precursor, respectively.

The electrochemical performance and lithium-storage behaviour of NiSb@NCNFs were systematically studied. Cyclic voltammetry (CV) analysis of NiSb@NCNFs was performed at a scan rate of 0.2 mV s^{-1} between 3.0 and 0.01 V *vs.* Li/Li^+ (Fig. 3a). In the 1^{st} discharge process (cathodic sweep), a broad reduction peak was presented between 1.0 and 0.3 V, which should be attributed to both the formation of the SEI film and the electrochemical reactions of NiSb. In the subsequent cathodic scans, a peak located at ~0.45 V emerged, which should be ascribed to the formation of Li_3Sb. In the anodic scans, only the well-defined peaks located at ~1.03 V appeared, owing to the delithiation of Li_3Sb. Notably, all the CV curves are almost overlapped except the 1^{st} cycle, implying the reversible electrochemical process and stable cycling performance of the NiSb@NCNF electrode. Fig. 3b displays the typical galvanostatic discharge/charge profiles of NiSb@NCNFs at a current density of 100 mA g^{-1}. The obvious potential plateau at ~1.0 V in the 1^{st} discharge scan was replaced by a slope in the subsequent cycles, which is consistent with the above CV results. The discharge curves are well overlapped from the 2^{nd} cycle to the 40^{th} cycle, implying the good cyclic performance of the NiSb@NCNF electrode.

The cycling performance of NiSb@NCNFs was measured at a current density of 100 mA g^{-1} (Fig. 3c). As two control samples, Ni and Sb nanocrystal embedded NCNFs (Ni@NCNFs and Sb@NCNFs, as detailed in the Experimental section) were also prepared and tested. The initial discharge capacity of the NiSb@NCNF electrode reaches 1220 mA h g^{-1}, and then decreases to 773 mA h g^{-1} at the 2^{nd} cycle. After 50 cycles, the

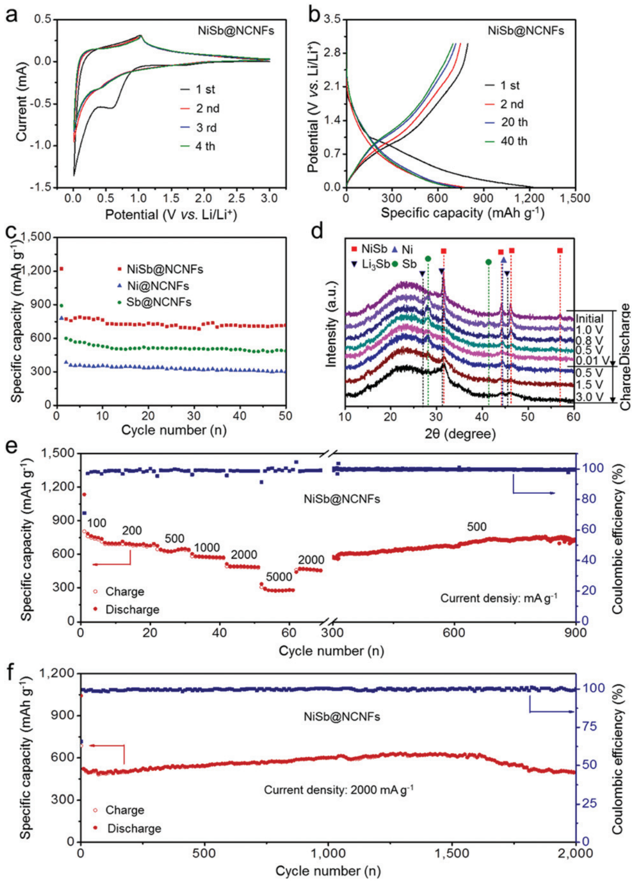

Fig. 3 (a) CV curves of NiSb@NCNFs between 3.0 and 0.01 V *vs.* Li/Li$^+$ at 0.2 mV s^{-1}. (b) Discharge/charge profiles of NiSb@NCNFs at a current density of 100 mA g^{-1}. (c) Discharge capacities of NiSb@NCNF, Ni@NCNF and Sb@NCNF electrodes at 100 mA g^{-1}. (d) *Ex situ* XRD spectra of NiSb@NCNFs during discharge/charge processes. (e) Rate performance of the NiSb@NCNF electrode at different current rates. (f) Long-term cycling performance and the corresponding coulombic efficiencies of the NiSb@NCNF electrode at a high current rate of 2000 mA g^{-1}.

discharge capacity still remains at 720 mA h g^{-1}, corresponding to a capacity retention of 93.4% to the 2$^{\text{nd}}$ cycle. The NiSb@NCNF electrode shows much higher discharge capacity and better cycling performance than Ni@NCNF and Sb@NCNF electrodes (302 and 488 mA h g^{-1} after 50 cycles, respectively), which should be attributed to the different lithium storage mechanisms of those electrodes. In detail, the Ni nanoparticles in Ni@NCNFs usually possess large particle sizes and may not be completely embedded into the NCNFs (Fig. S3a, b and S4a†). More importantly, the Ni@NCNF electrode shows almost no lithium storage behavior, as evidenced by the electrochemical tests in Fig. S5a.† On the other hand, the Sb nanoparticles in Sb@NCNFs would pulverize during continuous charging–discharging processes, which could increase the resistance of the Sb@NCNF electrode and lower the utilization ratio of the active material (Fig. S3c, d, S4b and S5b†). While for the NiSb@NCNF electrode, the introduction of Ni species and the dealloying–realloying cycles of the NiSb alloy can alleviate the volume expansion and prevent the aggregation of Sb particles, and effectively enhance the electronic conductivity of the NiSb@NCNF electrode (Fig. S6†). Therefore, the utilization of the NiSb alloy as an active material can take full advantage of Ni and Sb species, resulting in much better electrochemical performance than that of both Ni@NCNFs and Sb@NCNFs. The lithium storage performances of other control samples with different molar ratios and contents of Ni and Sb are discussed in the ESI (Fig. S7 and S8†), and all the results demonstrate the highest electrochemical performance of the NiSb@NCNF electrode.

To figure out the lithium storage mechanism of the NiSb@NCNF electrode, *ex situ* XRD measurements were performed at different discharge–charge stages. As presented in Fig. 3d, as the NiSb@NCNF electrode was discharged to 1.0 V, new diffraction peaks belonging to Ni and Sb emerged, suggesting the dealloying of NiSb. After discharging to 0.01 V, the diffraction peaks of the NiSb alloy and Sb disappeared, demonstrating the full dealloying of NiSb and the lithiation of Sb, while the diffraction peak belonging to Ni still remained. However, no expected diffraction peaks of Li_3Sb were found, which should be ascribed to the formation of amorphous Li_3Sb.[48,49] To further confirm that the NiSb@NCNFs reacted with Li$^+$ ions upon discharging, we characterized the present state of lithium in the NiSb@NCNF electrode after discharging to 0.01 V. As shown in Fig. S9,† the high-resolution XPS spectrum in the Li 1s region can be deconvoluted to two peaks centered at 54.8 and 55.7 eV, respectively. The peak located at 54.8 eV should be assigned to Li alloyed with Sb, and the other is ascribed to Li in the electrolyte decomposition products.[50] During the charging process from 0.5 V to 1.5 V, the diffraction peaks of Sb appeared firstly, indicating the delithiation of Li_3Sb. When further charging to 3.0 V, the diffraction peaks of Sb and Ni disappeared, while the peaks of NiSb emerged again, confirming the re-alloying of Ni and Sb to form NiSb. Therefore, the reversible lithium storage behavior of NiSb can be determined to be a special "dealloying–lithiation/delithiation–realloying" cyclic mechanism, as summarized below:

$$\mathrm{NiSb} \leftrightarrow \mathrm{Ni} + \mathrm{Sb} \tag{1}$$

$$\mathrm{Ni} + \mathrm{Sb} + 3\mathrm{Li} \leftrightarrow \mathrm{Ni} + \mathrm{Li_3Sb} \tag{2}$$

The dealloying process should be assigned to the transition stage that the lithium ions interacted with NiSb to form Ni and Sb, and then finally Ni and Li_3Sb. Therefore, the Sb dealloyed from NiSb could be regarded as an intermediate product of the NiSb lithiation process. It shall be noted that the Ni species play a crucial role during the lithiation/delithiation processes. Firstly, Ni can serve as the crystallic "host" for the realloying of NiSb, and buffer the volume change and prevent crumbling of Sb during discharge–charge cycles. Moreover, the high conducitivity of the NiSb alloy is conducive to maintain a good electrical contact between the embedded nanoparticles and NCNFs, and enable the full utilization of active materials.[51,52] This was experimentally confirmed by the electrochemical impedance spectroscopy (EIS) analysis in

Fig. S6,† which shows the lowest charge-transfer resistance of the NiSb@NCNF electrode compared to those of Ni@NCNF and Sb@NCNF electrodes.

The respective contributions of NiSb and NCNFs to the total discharge capacity were investigated. As shown in Fig. S10a,† the NiSb@NCNF electrode presented a high initial discharge capacity of 1062 mA h g^{-1} at a current density of 1000 mA g^{-1}, and then it remained almost stable in the following cycles. Eventually, a high reversible capacity of 610 mA h g^{-1} was still achieved at the 100th cycle. The NCNF electrodes deliver discharge and charge capacities of 759 and 494 mA h g^{-1} in the initial cycle at a current density of 1000 mA g^{-1}. The irreversible capacities are ascribed to the formation of the SEI layer. The discharge capacity decreases to 238 mA h g^{-1} in the 10th cycle and thereafter remains at 247 mA h g^{-1} after 300 cycles. Likewise, when tested at a low current density of 100 mA g^{-1}, the NCNF electrodes present a high discharge capacity of 958 mA h g^{-1}, and the reversible charge capacity is 650 mA h g^{-1} in the initial cycle, corresponding to a coulombic efficiency of 68%. The discharge capacity decreases to 421 mA h g^{-1} after 10 cycles and remains at 462 mA h g^{-1} after 100 cycles. The improved capacity of NiSb@NCNF electrodes should be attributed to the synergetic effect of the well dispersed NiSb nanoparticles and highly conductive NCNFs with lots of electrochemically active sites.

To characterize the morphology and microstructure variations of the NiSb@NCNF electrode, SEM and TEM were performed after 100 discharge–charge cycles at 1000 mA g^{-1}. As shown in Fig. S10c,† the outer surface of the NiSb@NCNF electrode is covered by the SEI film formed during cycling. The HRTEM image (Fig. S10d†) displays that the thickness of the SEI layer is ~4 nm. If without the encapsulation of NCNFs, the NiSb nanoparticles would be exposed to the electrolyte, and the SEI film would directly form and break on the surface of NiSb, resulting in poor electrochemical performance, especially low coulombic efficiencies. With the protection of the NCNFs, the SEI film was formed onto the outer surface of NiSb@NCNFs, and thus greatly increased the cycling stability.

Fig. 3e displays the rate performance of the NiSb@NCNF electrode at the current densities from 100 to 5000 mA g^{-1}. The initial coulombic efficiency is 71% at 100 mA g^{-1}. The NiSb@NCNF electrode exhibited a high discharge capacity of 750 mA h g^{-1} at 100 mA g^{-1}. On further increasing the current density to 200, 500, 1000, 2000 and 5000 mA g^{-1}, the discharge capacities remained at 690, 629, 581, 493 and 280 mA h g^{-1}, respectively, indicating good rate performance. When the current density recovered to 2000 mA g^{-1}, the discharge capacity was restored to 473 mA h g^{-1}. The NiSb@NCNF electrode maintained a high discharge capacity of 725 mA h g^{-1} after 900 cycles at 500 mA g^{-1}, showing high cycling stability. The increment of reversible capacity for the NiSb@NCNF electrode is attributed to the progressive activation process of the NiSb@NCNF electrode, which can also be found in other alloy based electrode materials of LIBs.[53]

The long-term cycling performance of the NiSb@NCNF electrode was tested at 2000 mA g^{-1}, as shown in Fig. 3f. The initial discharge capacity of NiSb@NCNFs reached 1043 mA h g^{-1}, and thereafter decreased to 520 mA h g^{-1} at the 9th cycle. In the following process, the discharge capacity gradually increased to 617 mA h g^{-1} after 1600 cycles, and then decreased to 510 mA h g^{-1} at the 2000th cycle. The coulombic efficiencies were also close to 100% during the entire 2000 cycles, indicating the high cycling stability and reversibility of the NiSb@NCNF electrode. The remarkably high reversible capacity and cycling stability of the NiSb@NCNF anode are mainly ascribed to the favorable synergistic effect between the 3D-interconnected NCNF network and NCNF-encapsulated NiSb nanoparticles. The carbon outer shell of NCNFs around NiSb nanoparticles is very helpful for the formation of a stable SEI film during the charge/discharge process; therefore the fracture of the SEI film during cycling can be prevented, resulting in excellent cycling stability. Furthermore, the carbon wall of NCNFs with high mechanical flexibility can provide efficient protection and inhibit the aggregation of NiSb nanoparticles, which is also very beneficial to the cycling stability. The tiny NiSb nanoparticles homogeneously dispersed in the NCNF can lead to a large contact area with the electrode and electrolyte, which can facilitate the transport of Li^+ ions into the interior of NiSb nanoparticles. Moreover, the highly conductive network of interlaced NCNFs is also conductive to the electron transfer of the electrode. These merits are the origins of the highly reversible storage capability of the NiSb@NCNF electrode.

Further studies were performed to figure out the origin of the high specific capacity of the NiSb@NCNF electrode. The total capacity of the electrode originated from the diffusion contribution and the capacitive contribution. To further determine the ratios of these two contributions, CV analysis was conducted to investigate the relationship between the scan rate (v) and measured current (i),[54] according to the following equations:

$$i\ (\mathrm{V}) = av^{b} \tag{3}$$

$$\lg i\ (\mathrm{V}) = b \lg v + \lg a \tag{4}$$

where i, v, a and b are the measured current, the scan rate and the adjustable parameters, respectively. According to the previous studies,[55,56] if b is close to 0.5, the electrode is controlled by a semi-infinite diffusion process; if b is approaching 1.0, the electrode is dominated by a capacitive response. Fig. S11a and b† show the CV curves and the calculated b-values of the NiSb@NCNF electrode. When the potential is varied from 0.1–1.2 V during the cathodic processes, the b-values are in the range of 0.6–0.8, indicating that both the diffusion and capacitive responses contribute to the total capacity. The b-values are 0.581 and 0.585 at the potentials of 1.0 and 1.1 V during the anodic processes, respectively, indicating that the discharge capacity mainly comes from the diffusion process. However, at higher potentials, the b-values increase to 0.65–0.95, suggesting that the capacitive response is dominated. Furthermore, the capacitive current and the diffusion controlled current can be quantitatively distinguished according to the following equations:[57,58]

$$i\ (\mathrm{V}) = k_1 \nu^{1/2} + k_2 \nu \tag{5}$$

$$i\ (\mathrm{V})/\nu^{1/2} = k_1 + k_2 \nu^{1/2} \tag{6}$$

where the parameters k_1 and k_2 can be calculated from the plots of i (V)/$\nu^{1/2}$ *vs.* $k_2\nu^{1/2}$. Thus, the capacitive contribution i (V)$_C$ = $k_2\nu$ can be distinguished from the total measured current with the value of k_2. As shown in Fig. S11c,† the diffusion controlled charge is mainly generated around the peak voltage in both anodic and cathodic processes, and contributes around 45.6% (~54.4% for capacitive, in the red region) of the total current at a scan rate of 0.8 mV s^{-1}. Along with the increase of the scan rate, the capacitive contribution increases gradually (37.5%, 39.7%, 51.2%, 54.4%, and 58.5% for 0.2, 0.4, 0.6, 0.8, and 1.0 mV s^{-1}, respectively), as shown in Fig. S11d.† These results confirm that both the diffusion and capacitive contributions account for the high specific capacity of NiSb@NCNFs, making the total capacity higher than the theoretical capacity of NiSb itself. The high specific capacity should be attributed to the well-dispersed small NiSb alloy nanoparticles and highly conductive mesoporous NCNFs, which provided lots of additional electrochemically active sites for lithium ion storage based on capacitive contribution, and a similar phenomenon was also reported in other previous studies.[59–63]

Since the freestanding NiSb@NCNF electrode shows good flexibility (Fig. 4a and b) and conductivity, it can be used as the anode in flexible Li-ion batteries. Fig. 4c presents the typical configuration of the soft-packed full batteries based on the NiSb@NCNF anode and LiFePO$_4$ cathode. The testing voltage window of the soft-packed full batteries was fixed at 0.9–4.0 V. Notably, most of the discharge capacities were generated above 2.4 V (Fig. S12†), suggesting the good potential in practical applications. Fig. 4d displays the cycling performance of the soft-packed full battery at 0.5C (1C = 170 mA h g^{-1}). The initial discharge capacity reached 136 mA h g^{-1} (calculated based on the loading mass of LiFePO$_4$ because the full cell was cathode limited), corresponding to an initial coulombic efficiency of 87%, and thereafter remained almost stable during the following cycles. The initial coulombic efficiency of the full battery (87%) is higher than that of the half-cell (71%), which should be ascribed to the prelithiation of the NiSb@NCNF electrode before cell assembling. The areal energy density of the NiSb@NCNF electrode can be calculated to be ~2142 mWh cm^{-2} (based on the NiSb@NCNF electrode) in a potential window of 0.9–4.0 V. The discharge capacity still remained at 118 mA h g^{-1} at the 100th cycle, corresponding to a capacity retention of 86.8%, indicating the good cycling stability. The capacity degradation was mainly attributed to the degradation of the cathode material based on commercial LiFePO$_4$, which also occurred in other soft-packed LIB systems.[64] The soft-packed full battery was then employed to light up a light-emitting-diode (LED) lamp under continuous bending and unbending states (Fig. 4e and f). The soft-packed battery can well illuminate the LED lamp under continuous bending and unbending states with no visual disparity, further demonstrating the good flexibility and robustness upon curving.

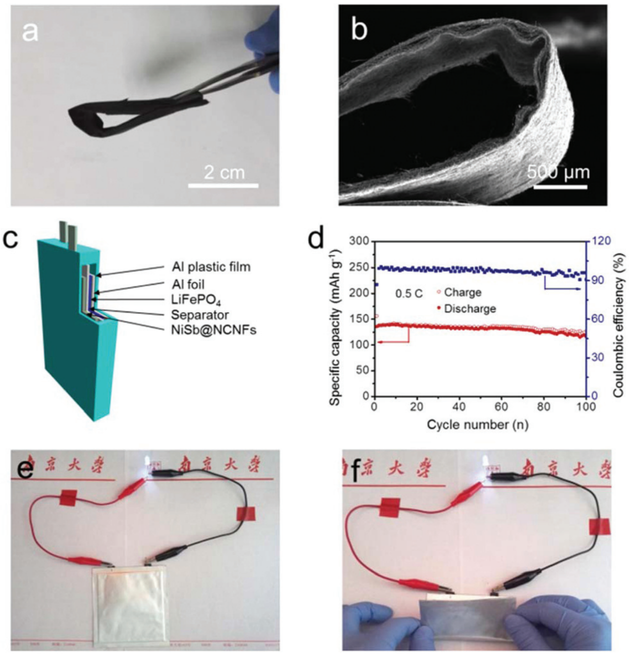

Fig. 4 (a) Optical photograph and (b) SEM image of the bent NiSb@NCNF electrode. (c) Schematic illustration of the soft-packed full battery assembled with a freestanding NiSb@NCNF anode and LiFePO$_4$ based cathode. (d) Cycling performance of the as-prepared soft-packed full battery. (e and f) Photographs of a LED lamp lighted up by the soft-packed full battery under bending-unbending states.

Conclusions

In summary, a freestanding NiSb@NCNF electrode was fabricated by encapsulating breithauptite nanoparticles into flexible NCNFs as a novel composite anode material for LIBs. Through detailed *ex situ* characterization, the reversible lithium storage behavior of NiSb@NCNFs was shown to follow a special "dealloying–lithiation/delithiation–realloying" cycling mechanism. Benefitting from the well-dispersed nano-sized NiSb nanoparticles, 3D highly conductive networks and restricted volume expansion by Ni species, the NiSb@NCNF electrode delivered high specific capacities and rate capability and long-term cycling stability at high rates. Moreover, the soft-packed full battery based on the NiSb@NCNF anode exhibits good flexibility and stability. This work provides a feasible strategy to achieve superb electrochemical performance of the Sb-based composite anode for LIBs.

Conflicts of interest

The authors declare no competing financial interest.

Acknowledgements

This work was supported by the National Key R&D Program of China (2017YFA0208200, 2016YFB0700600, and 2015CB659300), Projects of the NSFC (21872069, 51761135104, and 21573108), the Natural Science Foundation of Jiangsu Province (BK20180008), High-Level Entrepreneurial and Innovative Talents Program of Jiangsu Province, and the Fundamental Research Funds for the Central Universities of China.

Notes and references

1 F. Cheng, J. Liang, Z. Tao and J. Chen, *Adv. Mater.*, 2011, **23**, 1695–1715.

2 N. A. Kaskhedikar and J. Maier, *Adv. Mater.*, 2009, **21**, 2664–2680.

3 J. M. Tarascon, N. Recham, M. Armand, J. N. Chotard, P. Barpanda, W. Walker and L. Dupont, *Chem. Mater.*, 2010, **22**, 724–739.

4 A. Manthiram, K. Chemelewski and E. S. Lee, *Energy Environ. Sci.*, 2014, **7**, 1339–1350.

5 Y. Tang, Y. Zhang, W. Li, B. Ma and X. Chen, *Chem. Soc. Rev.*, 2015, **44**, 5926–5940.

6 M. K. Song, Y. Zhang and E. J. Cairns, *Nano Lett.*, 2013, **13**, 5891–5899.

7 B. Scrosati, J. Hassoun and Y. K. Sun, *Energy Environ. Sci.*, 2011, **4**, 3287–3295.

8 L. Mao, Q. Meng, A. Ahmad and Z. Wei, *Adv. Energy Mater.*, 2017, **7**, 1700535.

9 W. Liu, J. Chen, Z. Chen, K. Liu, G. Zhou, Y. Sun, M. Song, Z. Bao and Y. Cui, *Adv. Energy Mater.*, 2017, **7**, 1701076.

10 T. Gu, Z. Cao and B. Wei, *Adv. Energy Mater.*, 2017, **7**, 1700369.

11 H. Chang and H. Wu, *Energy Environ. Sci.*, 2013, **6**, 3483–3507.

12 J.-M. Tarascon and M. Armand, *Nature*, 2001, **414**, 359–367.

13 J. Cabana, L. Monconduit, D. Larcher and M. R. Palacin, *Adv. Mater.*, 2010, **22**, E170.

14 S. Y. Hong, Y. Kim, Y. Park, A. Choi, N.-S. Choi and K. T. Lee, *Energy Environ. Sci.*, 2013, **6**, 2067–2081.

15 Y. Li, B. Tan and Y. Wu, *Nano Lett.*, 2008, **8**, 265–270.

16 J. Liu, X. Xu, R. Hu, L. Yang and M. Zhu, *Adv. Energy Mater.*, 2016, **6**, 1600256.

17 S. Brutti, V. Gentili, H. Menard, B. Scrosati and P. G. Bruce, *Adv. Energy Mater.*, 2012, **2**, 322–327.

18 J. Chen, W. X. Song, H. S. Hou, Y. Zhang, M. J. Jing, X. N. Jia and X. B. Ji, *Adv. Funct. Mater.*, 2015, **25**, 6793–6801.

19 X. Zhou, L. Yu and X. W. D. Lou, *Adv. Energy Mater.*, 2016, **6**, 1600451.

20 N. Liu, Z. Lu, J. Zhao, M. T. McDowell, H.-W. Lee, W. Zhao and Y. Cui, *Nat. Nanotechnol.*, 2014, **9**, 187–192.

21 J. Liu, K. Song, C. Zhu, C.-C. Chen, P. A. van Aken, J. Maier and Y. Yu, *ACS Nano*, 2014, **8**, 7051–7059.

22 Y. Yu, L. Gu, C. Wang, A. Dhanabalan, P. A. van Aken and J. Maier, *Angew. Chem., Int. Ed.*, 2009, **121**, 6607–6611.

23 Y. Xu, Y. Zhu, Y. Liu and C. Wang, *Adv. Energy Mater.*, 2013, **3**, 128–133.

24 Y. L. Ding, C. Wu, P. Kopold, P. A. van Aken, J. Maier and Y. Yu, *Small*, 2015, **11**, 6026–6035.

25 N. Wang, Z. Bai, Y. Qian and J. Yang, *Adv. Mater.*, 2016, **28**, 4126–4133.

26 K. Xu, *Chem. Rev.*, 2004, **104**, 4303–4418.

27 K. Xu and A. von Cresce, *Chem.*, 2011, **21**, 9849–9864.

28 D. Aurbach, *J. Power Sources*, 2000, **89**, 206–218.

29 C. Villevieille, C.-M. Ionica-Bousquet, B. Ducourant, J.-C. Jumas and L. Monconduit, *J. Power Sources*, 2007, **172**, 388–394.

30 J. Xie, X. Zhao, H. Yu, H. Qi, G. Cao and J. Tu, *J. Alloys Compd.*, 2007, **441**, 231–235.

31 J. L. Gómez-Cámer, C. Villevieille and P. Novák, *J. Mater. Chem. A*, 2013, **1**, 13011–13016.

32 J. Xie, X. Zhao, G. Cao, M. Zhao and S. Su, *J. Power Sources*, 2005, **140**, 350–354.

33 J. Xie, X. Zhao, G. Cao, Y. Zhong, M. Zhao and J. Tu, *Electrochim. Acta*, 2005, **50**, 1903–1907.

34 Y. Yang, F. Liu, T. Li, Y. Chen, Y. Wu and M. Kong, *Scr. Mater.*, 2012, **66**, 495–498.

35 J. Xu, H. Wu, F. Wang, Y. Xia and G. Zheng, *Adv. Energy Mater.*, 2013, **3**, 286–289.

36 H. Hou, X. Cao, Y. Yang, L. Fang, C. Pan, X. Yang, W. Song and X. Ji, *Chem. Commun.*, 2014, **50**, 8201–8203.

37 E. Allcorn and A. Manthiram, *J. Phys. Chem. C*, 2014, **118**, 811–822.

38 D. Applestone, S. Yoon and A. Manthiram, *J. Mater. Chem.*, 2012, **22**, 3242–3248.

39 E. Allcorn and A. Manthiram, *ACS Appl. Mater. Interfaces*, 2014, **6**, 10886–10891.

40 B. Koo, H. Kim, Y. Cho, K. T. Lee, N. S. Choi and J. Cho, *Angew. Chem., Int. Ed.*, 2012, **51**, 8892–8897.

41 Y. Du, X. Zhu, L. Si, Y. Li, X. Zhou and J. Bao, *J. Phys. Chem. C*, 2015, **119**, 15874–15881.

42 C. Kim, K. S. Yang, M. Kojima, K. Yoshida, Y. J. Kim, Y. A. Kim and M. Endo, *Adv. Funct. Mater.*, 2006, **16**, 2393–2397.

43 Y. C. Liu, N. Zhang, C. M. Yu, L. F. Jiao and J. Chen, *Nano Lett.*, 2016, **16**, 3321–3328.

44 Y. H. Xu, Y. J. Zhu, F. D. Han, C. Luo and C. S. Wang, *Adv. Energy Mater.*, 2015, **5**, 1400753.

45 X. Y. Wang, L. Fan, D. C. Gong, J. Zhu, Q. F. Zhang and B. Lu, *Adv. Funct. Mater.*, 2016, **26**, 1104–1111.

46 L. Ji, M. Gu, Y. Shao, X. Li, M. H. Engelhard, B. W. Arey, W. Wang, Z. Nie, J. Xiao and C. Wang, *Adv. Mater.*, 2014, **26**, 2901–2908.

47 M. Zhang, E. Uchaker, S. Hu, Q. Zhang, T. Wang, G. Cao and J. Li, *Nanoscale*, 2013, **5**, 12342–12349.

48 J. Ding, H. Zhou, H. Zhang, L. Tong and D. Mitlin, *Adv. Energy Mater.*, 2018, **8**, 1701918.

49 W. Luo, J. Gaumet and L. Mai, *Rare Met.*, 2017, **36**, 321–338.

50 F. Martin, J. Morales and L. Sanchez, *ChemPhysChem*, 2008, **9**, 2610–2617.

51 Y. Mai, J. Tu, C. Gu and X. Wang, *J. Power Sources*, 2012, **209**, 1–6.

52 B. Wang, J. Cheng, Y. Wu, D. Wang and D. He, *J. Mater. Chem. A*, 2013, **1**, 1368–1373.

53 J. Qin, C. He, N. Zhao, Z. Wang, C. Shi, E. Liu and J. Li, *ACS Nano*, 2014, **8**, 1728–1738.

54 T. Brezesinski, J. Wang, J. Polleux, B. Dunn and S. H. Tolbert, *J. Am. Chem. Soc.*, 2009, **131**, 1802–1809.

55 P. Yu, C. Li and X. Guo, *J. Phys. Chem. C*, 2014, **118**, 10616–10624.

56 K. Zhu, Q. Wang, J.-H. Kim, A. A. Pesaran and A. J. Frank, *J. Phys. Chem. C*, 2012, **116**, 11895–11899.

57 V. Augustyn, J. Come, M. A. Lowe, J. W. Kim, P. L. Taberna, S. H. Tolbert, H. D. Abruna, P. Simon and B. Dunn, *Nat. Mater.*, 2013, **12**, 518–522.

58 C. Chen, Y. Wen, X. Hu, X. Ji, M. Yan, L. Mai, P. Hu, B. Shan and Y. Huang, *Nat. Commun.*, 2015, **6**, 6929.

59 J. Li, X. Xu, Z. Luo, C. Zhang, Y. Zuo, T. Zhang, P. Tang, M. Infante-Carrio, J. Arbiol, J. Llorca, J. Liu and A. Cabot, *ChemSusChem*, 2019, **12**, 1–9.

60 W. Guo, W. Sun and Y. Wang, *ACS Nano*, 2015, **9**, 11462–11471.

61 L. Shi, D. Li, H. Liu, Y. Zhao, H. Xin, Y. Lin, C. Lin, C. Li and C. Zhu, *J. Mater. Chem. A*, 2018, **6**, 7967–7976.

62 K. Cao, L. Jiao, Y. Liu, H. Liu, Y. Wang and H. Yuan, *Adv. Funct. Mater.*, 2015, **25**, 1082–1089.

63 J. Liu, C. Wu, D. Xiao, P. Kopold, L. Gu, P. van Aken, J. Maier and Y. Yan, *Small*, 2016, **12**, 2354–2364.

64 G. Zhu, L. Wang, H. Lin, L. Ma, P. Zhao, Y. Hu, T. Chen, R. Chen, Y. Wang, Z. Tie, J. Liu and Z. Jin, *Adv. Funct. Mater.*, 2018, **28**, 1800003.